



## Stochastic model for predicting the shape of flexible fibers in suspensions

Mona Rahmani <sup>1,\*</sup>, Arash Alizad Banaei<sup>2,3</sup>, Luca Brandt <sup>2,4</sup> and D. Mark Martinez<sup>1</sup>

<sup>1</sup>*Department of Chemical and Biological Engineering, The University of British Columbia,  
Vancouver, Canada V6T 1Z3*

<sup>2</sup>*Linné FLOW Centre and Swedish e-Science Research Centre, KTH, Department of Engineering Mechanics,  
SE-10044 Stockholm, Sweden*

<sup>3</sup>*PDC Center for High Performance Computing, KTH Royal Institute of Technology,  
SE-100 44 Stockholm, Sweden*

<sup>4</sup>*Department of Energy and Process Engineering, Norwegian University of Science and Technology,  
Trondheim NO-7491, Norway*



(Received 19 October 2021; accepted 31 January 2023; published 23 February 2023)

We describe the shape of moderately flexible fibers settling under inertial conditions in dilute and semidilute suspension and examine the hydrodynamic forces on the fibers that create different fiber shapes. The analysis is based on numerical simulations, using an immersed boundary method, to couple the motion of the fibers to the fluid dynamics. The direct numerical simulation results show that while fiber curvature can have a non-monotonic dependence on fiber concentration, fiber torsion monotonically increases with increasing the concentration of fibers. Based on the concept of splitting the total forces into a mean and a stochastic part, we propose a reduced-order, stochastic model that can, with a reasonable accuracy, model the three-dimensional fiber shapes at different fiber concentrations, flexibility, and inertia. This model also helps us understand how random hydrodynamic fluctuations and fluid-mediated forces due to the presence of neighboring fibers contribute to the total forces on the fibers and fiber shapes.

DOI: [10.1103/PhysRevFluids.8.024306](https://doi.org/10.1103/PhysRevFluids.8.024306)

### I. INTRODUCTION

In a suspension of settling flexible fibers, the shape of the fibers varies depending on the hydrodynamic interactions of each fiber with the flow, the fluid-mediated interactions with the neighboring fibers, and fiber-fiber contacts. Understanding the shapes that flexible fibers adopt in a suspension is important in many applications such as the pulp and paper industry [1], composite materials [2], biomaterials [3], and biological flows [4]. The shapes of the fibers significantly influence the properties of materials made from fiber networks [5], that often rely on the settling process as part of their manufacturing [6]. The effects of long-range interactions on the shape of flexible-body microorganisms, known for exploiting the advantages of collective swimming in suspensions [7], are crucial for their ability to overcome the gravitational force in environmental flows [8]. While the shape of a single flexible fiber settling in a viscous flow has been studied in the past (e.g., see [9] for a review), this paper examines the shape of settling flexible fibers in a suspension.

The shapes that fibers take in a suspension depend on different parameters, such as fiber concentration, fiber flexibility, the density ratio between the fibers and the suspending fluid, the fiber aspect ratio, and the viscosity of the fluid. Most studies of the shape of settling flexible fibers

---

\*Corresponding author: [mona.rahmani@ubc.ca](mailto:mona.rahmani@ubc.ca)

have focused on the settling of a single fiber in a viscous flow [10–16]. These studies have shown that as the bending rigidity of the fibers decreases, the fiber bending increases and finally saturates, while the fiber shape transitions from V shaped to U shaped and occasionally W shaped. Isolated flexible fibers in a turbulent flow can, however, adopt more complex shapes with multiple inflection points, or buckle, depending on the fiber length, flexibility, and turbulence intensity [17–22]. In shear flows, a single fiber can curl to shapes with high local curvatures [23]. In compressional flows, a single straight flexible fiber can even buckle into helical shapes [24]. Proximity to a rough wall can also induce more bending of flexible fibers [25]. Simulations of two or three settling flexible fibers in viscous flows have revealed that the fiber-fiber interaction modifies the shape and orientation of settling fibers [15,26].

In suspensions with many flexible fibers, the shape and bending of flexible fibers influence the shear viscosity of fiber suspensions [27], mechanical entanglement [28], flocculation [29], and the diffusion coefficient [30] of fibers. The knowledge of shape of flexible fibers in suspensions is however very limited. In the past, several studies have focused on the orientation of rigid fibers in suspensions [31–35], or clustering patterns of settling rigid fibers [36–38] and settling weakly flexible fibers [12,39,40]. For a suspension of settling fibers, in a previous study [29] we have shown that flexible fibers bend more as the concentration of fibers in the suspension increases. In a channel flow, Dotto and Marchioli [41] and Dotto *et al.* [42] showed that the fibers' bending depends on the location of the fibers with respect to the wall and the aspect ratio of the fibers. In the laboratory experiments of fiber suspensions in a channel flow by Alipour *et al.* [43], the local curvature of flexible fibers controlled the rotation rate and orientation of the fibers. For a suspension of dilute fibers in a homogeneous, isotropic turbulence, Sulaiman *et al.* [44] demonstrated that the fiber deformation can be characterized by the ratio of fiber length to a length scale that measure the ratio of turbulence forcing to fiber flexibility.

In the present paper, our goal is to understand how the shapes of settling flexible fibers vary in suspensions of different concentrations. To this end, we consider a suspension of moderately flexible fibers, settling in an inertial regime, at different fiber concentrations that represent dilute and semidilute regimes. We consider two different values of the Galileo number, measuring the ratio of gravitational to viscous forces, and two different values of dimensionless fiber rigidity. First, we use direct numerical simulation (DNS) of the fluid phase, combined with an immersed boundary method for the coupling between the fluid and fiber phase, as detailed in previous studies [22,45–47]. Second, we use the data from our numerical simulations to propose a physics-based, reduced-order, stochastic model for predicting the shape of the fibers in different regimes. More specifically, our goal is to answer two fundamental questions.

(i) How do the average and stochastic parts of the forces on the fibers change due to increased fiber-fiber interactions at higher fiber concentration?

(ii) Can reduced-order models for fiber forces give an accurate account of the fiber shapes?

The decomposition of forces into an average and a stochastic part in the former question has been discussed in the literature for suspensions of spherical particles [48–51]. However, this decomposition is more complicated in the case of fibers, as the forces vary along the fiber length. Regarding our second question, analytical models have been used to find the shape of a weakly flexible fiber settling in a Stokes flow [52], and a flexible fiber fixed in a two-dimensional (2D) free-streamline flow [53]. Here, we are inspired by these studies to propose a model for finding the fiber shapes in three dimensions, and in situations where inertia and fiber-fiber interactions are significant. In this regard, we solve a simplified version of the Euler-Bernoulli equations, decomposed into the normal, tangential, and binormal directions, with modeled forcing applied to them.

We use the local fiber curvature, local fiber torsion, fiber end-to-end distance, fiber height, and fiber out-of-plane height as measures of fiber deformation. Deformation of flexible fiber is commonly quantified by the fiber end-to-end distance, either in numerical simulations [41,42,44] or experimental studies [18,21]. Local fiber curvature has also been used to measure the bending deformation of fibers both numerically [19] and experimentally [19,43]. However, apart from the microstructure studies of fiber assemblies for composite materials [54], the local torsion of the

fibers and the corresponding out-of-plane height have received less attention in the context of fibers suspended in a fluid.

The paper is organized as follows. We discuss the numerical results in Sec. II, discuss the stochastic model for forces on the fibers and finding fiber shapes in Sec. III, and state the conclusions in Sec. IV.

## II. NUMERICAL EXPERIMENTS

### A. Numerical formulation

The motion of a thin flexible and inextensible fiber is described by the Euler-Bernoulli beam equation under the constraint of inextensibility

$$\frac{\partial^2 \mathbf{X}}{\partial t^2} = \frac{\partial}{\partial s} \left( T \frac{\partial \mathbf{X}}{\partial s} \right) - \gamma \frac{\partial^4 \mathbf{X}}{\partial s^4} + \frac{1}{r} \frac{\mathbf{g}}{g} - \mathbf{F}_h + \mathbf{F}_c, \quad (1a)$$

$$\frac{\partial \mathbf{X}}{\partial s} \cdot \frac{\partial \mathbf{X}}{\partial s} = 1, \quad (1b)$$

and subject to zero torque, force, and tension boundary conditions at the free ends of the fiber:

$$\frac{\partial^2 \mathbf{X}}{\partial s^2} = 0, \quad (2a)$$

$$\frac{\partial^3 \mathbf{X}}{\partial s^3} = 0, \quad (2b)$$

$$T = 0, \quad (2c)$$

where  $\mathbf{X}$  is the fiber position,  $s$  is the curvilinear coordinate along the fibers,  $t$  is time,  $T$  is the dimensionless tension,  $\mathbf{F}_h$  is the fluid-fiber interaction force per unit length, and  $\mathbf{F}_c$  is the repulsive force used to model interactions between adjacent fibers. The parameter  $r \equiv \Delta\rho/\rho_0 = 0.1$  is the ratio of the density difference between fluid and the fibers,  $\Delta\rho$ , to the density of the base flow,  $\rho_0$ , and  $\mathbf{g}$  is the gravitational acceleration vector with the magnitude of  $g$ . For a fiber with length  $L$ , surface area  $A_f$ , flexural rigidity  $EI$ , settling due to its density difference  $\Delta\rho$  with respect to a suspending fluid density  $\rho_0$ , and thus experiencing a gravitational force  $F_g = \Delta\rho A_f L g$ , the dimensionless bending rigidity is  $\gamma = EI/(F_g L^2 \Delta\rho/\rho_0)$ , where fibers with lower  $\gamma$  are more flexible. To nondimensionalize Eqs. (1), we have used the following characteristic scales:  $L$  for the initial length of fibers for length scale,  $L/U_s$  for time scale where  $U_s = \sqrt{r g L}$  is a characteristic velocity scale,  $\rho_0 U_s^2$  for tension, and  $\rho_0 U_s^2/L$  for the gravitational, fluid-fiber interaction, and repulsive forces.

The equations of motion of the fluid phase are described by the incompressible Navier-Stokes equations, which in a Cartesian frame of reference, and in nondimensional form are expressed as

$$\frac{\partial \mathbf{u}}{\partial t} + \nabla \cdot (\mathbf{u} \otimes \mathbf{u}) = -\nabla p + \frac{1}{Ga} \nabla^2 \mathbf{u} + \mathbf{f}, \quad (3a)$$

$$\nabla \cdot \mathbf{u} = 0, \quad (3b)$$

where  $\mathbf{u}$  is the velocity field,  $p$  is the pressure,  $\mathbf{f}$  is a volume force from the action of fibers on the fluid, and  $Ga = \sqrt{g L^3 \Delta\rho/\rho_0}/\nu$  is the Galileo number, with  $\nu$  being the fluid kinematic viscosity. We solve Eqs. (1) and (3) numerically using a finite difference discretization on an Eulerian mesh  $\mathbf{x}$  for the fluid and a Lagrangian mesh  $\mathbf{X}$  for the fibers, where the fluid and solid motions are coupled using the immersed boundary method, as explained and validated in detail in our previous work [29,45].

TABLE I. Summary of the DNS simulations performed. In all the simulations, the fiber aspect ratio is  $r_p = 20$ , the domain size is  $(L_x, L_y, L_z) = (2\pi, 2\pi, 4\pi)$ , and the number of Eulerian grid points is  $(N_x, N_y, N_z) = (128, 128, 256)$ .

Simulation	$Ga$	$\gamma$	$nL^3$	Simulation	$Ga$	$\gamma$	$nL^3$	Simulation	$Ga$	$\gamma$	$nL^3$
1	160	0.1	0								
2	160	0.1	3	8	160	0.05	3				
3	160	0.1	7	9	160	0.05	7				
4	160	0.1	10	10	160	0.05	10	14	40	0.1	10
5	160	0.1	15	11	160	0.05	15	15	40	0.1	15
6	160	0.1	25	12	160	0.05	25	16	40	0.1	25
7	160	0.1	35	13	160	0.05	35	17	40	0.1	35

Our numerical model includes a lubrication force, and a repulsive force to simulate the short-range interactions and contacts between the fibers, respectively. The details of the hydrodynamic, contact, and lubrication forces used in our model are explained in the Appendix.

A summary of the simulations performed for this paper is given in Table I. In simulations 1–7, we consider a suspension of moderately flexible fibers, with  $\gamma = 0.1$ , settling at a Galileo number of  $Ga = 160$ , at different fiber concentrations. The simulations in this set (except for the  $nL^3 = 0$  and 35 simulations) overlap with the results published in our previous work [29], where we examined the effects of fiber concentration on settling velocity, fiber orientation, and end-to-end distance. The  $nL^3 = 0$  simulation represents the settling of a single fiber. Simulations 8–13 correspond to the settling of more flexible fibers, with  $\gamma = 0.05$ , at different fiber concentrations. In addition, we have conducted simulations 14–17 at  $Ga = 40$  to investigate the effects of inertia on fiber shape. Simulations 7, 13, and 17, with the highest fiber concentration of  $nL^3 = 35$ , will be used to test the extrapolation of our stochastic model. The ratio of fiber length to diameter in all the simulations is  $r_p = 20$ , and each fiber is discretized using 21 Lagrangian nodes. The domain size is  $(L_x, L_y, L_z) = (2\pi, 2\pi, 4\pi)$ , and the Eulerian grid size is  $(N_x, N_y, N_z) = (128, 128, 256)$ , with negative  $z$  being in the gravity direction. Triple periodic boundary conditions are applied, and the dimensionless time step is  $\Delta t = 0.0005$ . Initially, fibers are uniformly distributed in the domain with random locations and orientations. The statistically steady state of the fiber suspensions is independent of the initial state.

## B. Fiber frames of reference, curvature, and torsion

To quantify the shape of the fibers better, we consider the curvilinear coordinates in which the locations of the points on the fiber are given by a curve parametrized by the arc length  $s$  along the fiber:  $\mathbf{X}(s)$ , where  $\mathbf{X}'(s)$  satisfies the inextensibility condition,  $\mathbf{X}'(s) \cdot \mathbf{X}'(s) = 1$ . Then the Frenet frame on the fiber can be formed with the unit tangent vector, and the unit normal vector at  $s$  is defined as  $\mathbf{s}(s) = \mathbf{X}'(s)$  and  $\mathbf{n}(s) = \mathbf{X}''(s)$ , respectively [see Fig. 1(a)]. The unit binormal vector is found from  $\mathbf{t}(s) = \mathbf{s}(s) \times \mathbf{n}(s)$ . The fiber curvature at any local point is defined as  $\kappa(s) = |\mathbf{X}''(s)|$  and the fiber torsion at any local point is defined as  $\tau(s) = \mathbf{n}'(s) \cdot \mathbf{t}(s)$ . The curvature and torsion measure the fiber bending with respect to the normal and binormal directions, respectively. The curvature always has a positive sign, while the torsion can take either positive or negative signs. To facilitate comparisons of individual fibers, a new frame of reference  $(x', y', z')$  can be defined in the center of each fiber, where  $x'$ ,  $y'$ , and  $z'$  are the local tangent, binormal, and normal vectors, respectively. Using the Tait-Bryan angles between  $(x, y, z)$  and  $(x', y', z')$ , a rotation matrix is built that transforms the fiber location from the  $(x, y, z)$  frame to the  $(x', y', z')$  frame.

To quantify the shape of the fibers, we define three parameters, as illustrated in Fig. 1. Fiber end-to-end distance,  $d$ , is a measure of the bending of the fiber due to its curvature or torsion. The fiber height,  $h$ , measures the height of the fiber on the osculating plane and is defined as the largest

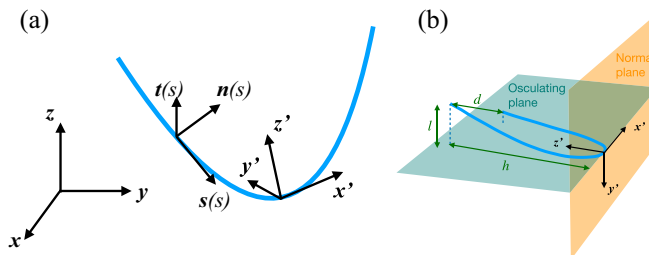


FIG. 1. (a) Different frames of reference for the fibers. (b) Schematic of the definition of the geometrical properties of a fiber in an  $(x', y', z')$  frame of reference.

absolute value of  $y'$  attained by all the points on the fiber. The out-of-plane fiber height,  $l$ , is the height of the fiber on the normal plane and is defined as the absolute value of the difference between the maximum and minimum  $z'$  for all the fiber points. The value of  $l$  will be zero if the fiber is planar.

### C. Direct numerical simulations results

In Fig. 2 we show the snapshots of the settling fibers at different fiber concentrations at two different values of fiber flexibility  $\gamma = 0.05$  and  $0.1$  at  $Ga = 160$ . In all the cases, the fibers adopt random orientation and different bending values (e.g., see our previous work [29] for more quantitative analysis of fiber orientation and bending at different fiber concentrations). However, as the fibers are moderately flexible, they mostly demonstrate nearly straight, V, or U shapes. Obviously, there are variations in the shape of the fibers and it can qualitatively be conjectured that the shape variations increase with increasing the fiber concentrations and fiber flexibility. In our previous work [29], we have shown that the concentration  $nL^3 = 3$  corresponds to a dilute regime, where the fiber-fiber interactions are important but the fiber clumping is insignificant, and the concentrations  $nL^3 = 10$  and  $25$  fall in a semidilute regime, where fibers significantly clump together and interact with each other. In the latter regime, the fiber-fiber interaction forces can play an important role in changing the shape of the fibers.

Shapes of all the fibers in the  $(x', y', z')$  frame, projected on the osculating and normal planes, in suspensions with different fiber concentrations are shown in Fig. 3 for  $\gamma = 0.1$  and in Fig. 4 for  $\gamma = 0.05$ . As the fiber concentration in the suspension increases, the fiber bending both in the osculating plane and in the normal plane increases. Decreasing the fiber rigidity from  $\gamma = 0.1$  to  $0.05$  also makes the fiber bending increase significantly. In the osculating plane, the vast majority of fibers are bent in the opposite direction of gravity (positive  $z'$ ), while as  $nL^3$  increases or as  $\gamma$  decreases, more fibers are bent in the direction of gravity. In the normal plane, however, the fiber bending does not demonstrate a preferred direction, which is expected due to symmetry.

In Fig. 5, we show the trends of variations of fiber curvature, fiber torsion, fiber height, fiber out-of-plane height, and fiber end-to-end distance with fiber concentration,  $nL^3$ , for three different data sets. In this figure, fiber curvature and torsions have been averaged over the fiber length (denoted by  $\langle \cdot \rangle$  in the rest of the paper), and also averaged over all the fibers in the domain (denoted by  $\bar{\cdot}$  in the rest of the paper), and the fiber heights and the end-to-end distances are averaged over all the fibers. The averaged fiber curvature has a nonmonotonic dependence on  $nL^3$ . The averaged curvature of a single fiber is considerably higher compared to suspensions. As  $nL^3$  increases, the averaged curvature decreases in the dilute regime,  $nL^3 < 10$ , as the settling velocity is hindered [29] and the hydrodynamic forces on the fiber are reduced. In the semidilute regime,  $nL^3 > 10$ , the rate of hindering of settling velocity slows down and the fiber-fiber interaction become more significant. In this regime, the averaged curvature slightly increases with increasing  $nL^3$ , except for

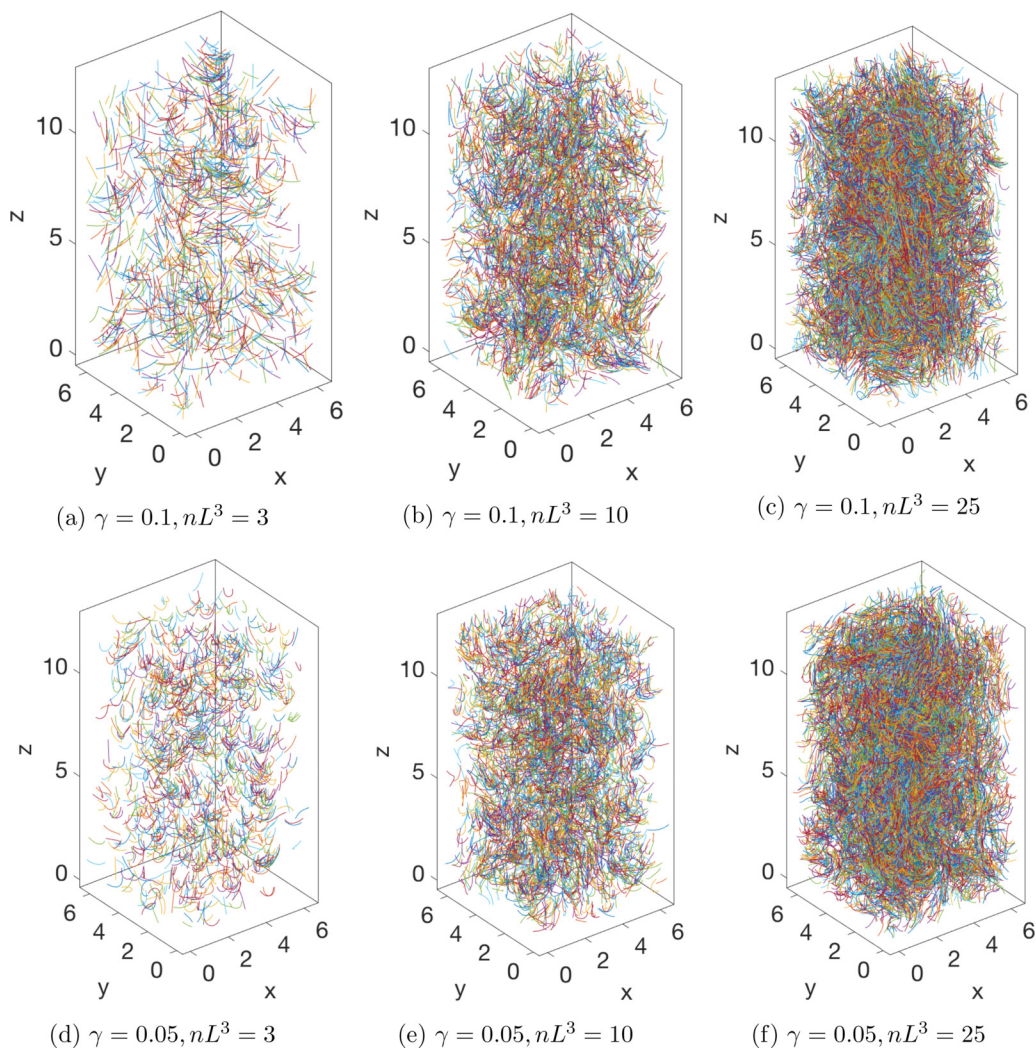


FIG. 2. Settling fiber suspensions at different fiber flexibility and concentrations at  $Ga = 160$ . The color map is a label for the individual fibers.

$nL^3 > 15$  at  $Ga = 160$  and  $\gamma = 0.1$  that shows a decreasing trend of  $\overline{\langle \kappa \rangle}$  with  $nL^3$ . Fiber heights are correlated with the fiber curvature, and both fiber height and curvature increase as fiber flexibility or the Galileo number increases. Averaged fiber torsion that is generated by the binormal forces is less dependent on the gravitational forces and more dependent on the fiber-fiber interaction forces. So as shown in Fig. 5(b), the averaged torsion increases monotonically with the fiber concentration and increases as the fiber flexibility rises, but does not reveal a significant dependence on the Galileo number. Fiber torsion and out-of-plane height exhibit the same trends. At  $Ga = 40$ , the fiber out-of-plane height values are lower compared to those at  $Ga = 160$ , although their averaged torsion values are the same. This is because the averaged fiber curvatures are higher at  $Ga = 160$  and this contributes to the fibers gaining larger out-of-plane heights with similar averaged torsion values. The variation of the averaged fiber end-to-end distance, a measure of the total deformation of fibers, with  $nL^3$  exhibits a closer correlation with the fiber heights rather than fiber out-of plane heights since the former in general attains higher values and contributes more to the total fiber deformation.

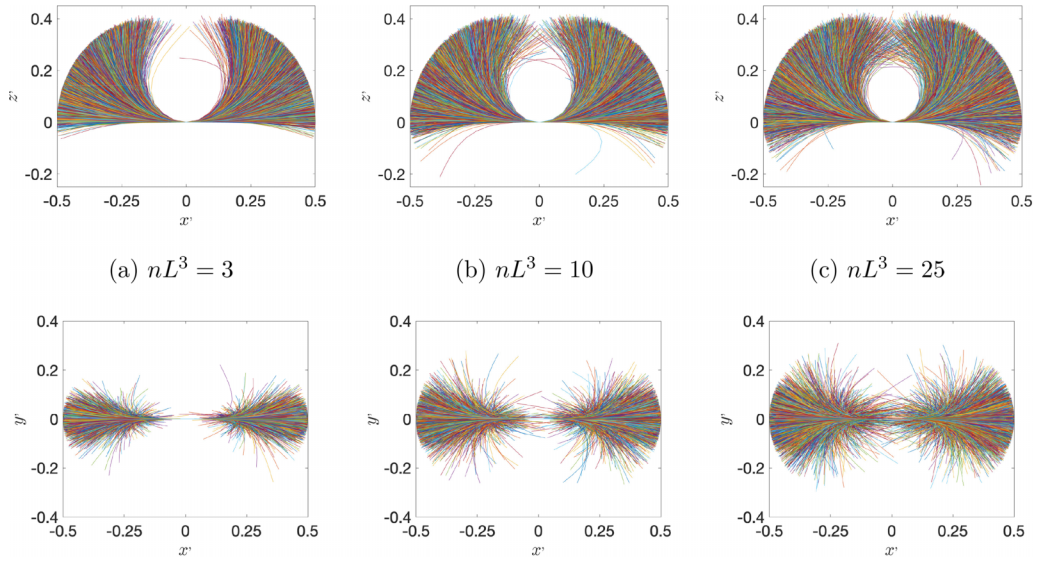


FIG. 3. The DNS fiber shapes (from 15 000 fibers in each case) projected on the osculating plane (top row) and projected on the normal plane (bottom row) for different fiber concentrations and  $\gamma = 0.1$  and  $Ga = 160$ . The color map is a label for the individual fibers.

Different fiber shapes at varying fiber concentrations and flexibility are due to the changing nature of hydrodynamic and fiber-fiber interaction forces. To investigate the force effects on fiber shapes, in the following section we propose a stochastic model that can predict the fiber shapes closely compared to DNS and help us understand how fiber forces change at different concentrations and fiber flexibility.

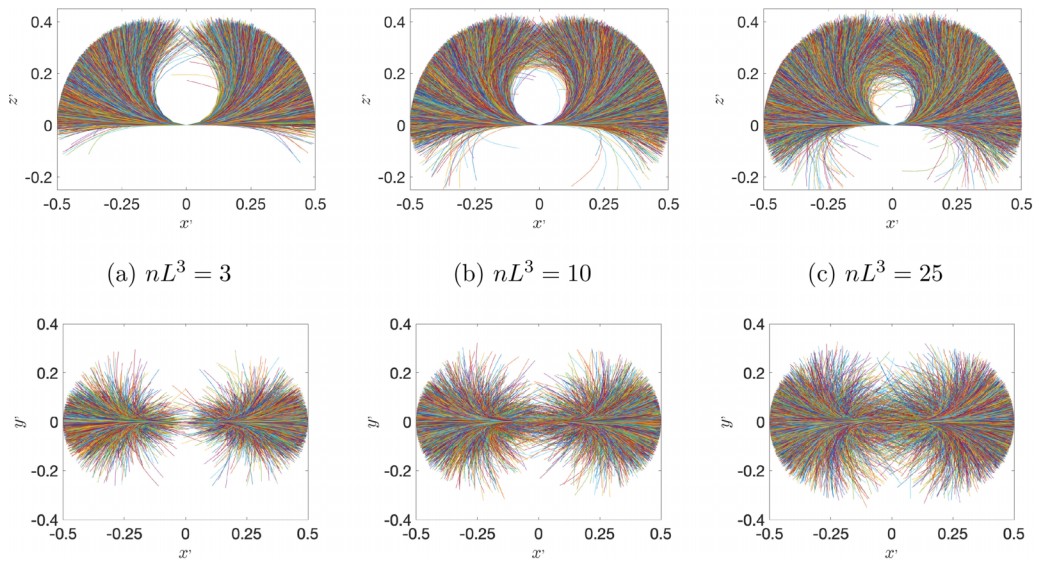


FIG. 4. The DNS fiber shapes (from 15 000 fibers in each case) projected on the osculating plane (top row) and projected on the normal plane (bottom row) for different fiber concentrations and  $\gamma = 0.05$  and  $Ga = 160$ . The color map is a label for the individual fibers.

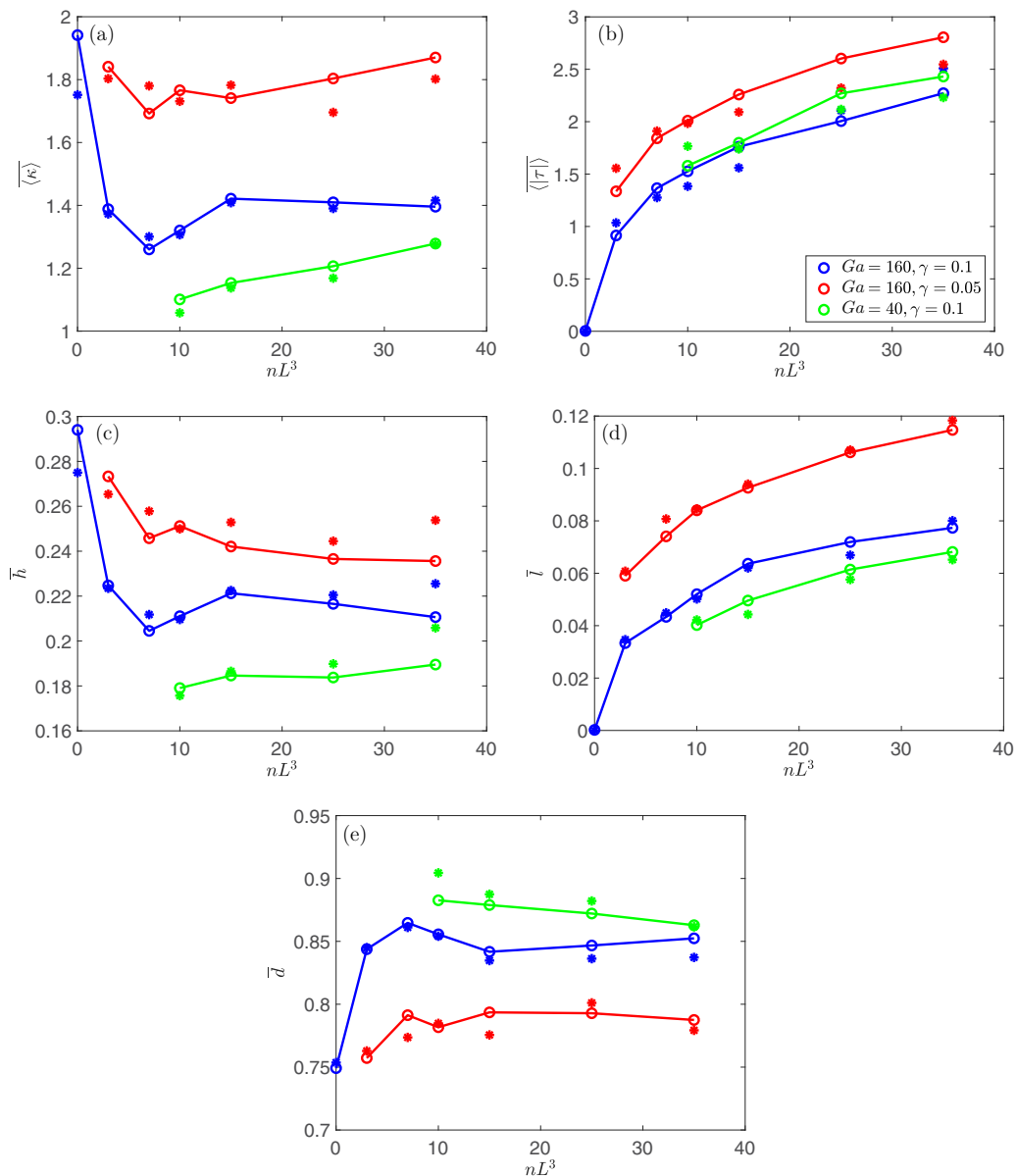


FIG. 5. Variation of averaged fiber curvature (a), torsion (b), height (c), out-of-plane height (d), and end-to-end distance (e) with  $nL^3$  for different data sets. The stars show the predictions of the stochastic model discussed in Sec. III, where the stars at  $nL^3 = 35$  delineate the predictions of the model with extrapolated empirical values.

### III. STOCHASTIC MODEL FOR FIBER SHAPES

To understand the shape of the flexible fibers better, we focus on answering the first question: how do the average and stochastic parts of the forces on the fibers change by increasing the fiber concentration? First, let us demonstrate how the forces on fibers determine their shapes. Assuming that the fibers on average have reached a statistically steady state, which is true when the bulk properties of fiber suspension are of interest, and using the normal vector relations, the first part of



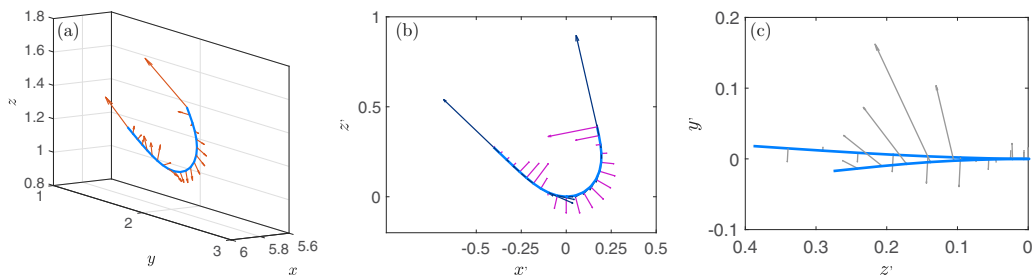


FIG. 6. (a) Distribution of forces on a fiber in the original frame of reference. (b), (c) Decomposition of forces into normal and tangential forces (b) and binormal forces (c). Scales are different between different panels.

Eqs. (1) can be simplified to

$$\frac{\partial}{\partial s}(Ts) - \gamma \frac{\partial^2}{\partial s^2}(\kappa \mathbf{n}) = \mathbf{F}, \quad (4)$$

where  $\mathbf{F}$  is the sum of hydrodynamic, fiber contact, and gravitational forces. After expanding Eq. (4), the force balance equations in the tangential, normal, and binormal directions are respectively derived as

$$T = -\frac{3}{2}\gamma\kappa^2 + \int_{-0.5}^{0.5} F_s ds, \quad (5)$$

$$\frac{\partial^2 \kappa}{\partial s^2} + \frac{1}{2}\kappa^3 - \kappa\tau^2 - \frac{\kappa}{\gamma} \int_{-0.5}^{0.5} F_s ds = -\frac{F_n}{\gamma}, \quad (6)$$

$$2\frac{\partial \kappa}{\partial s}\tau + \kappa\frac{\partial \tau}{\partial s} = -\frac{F_t}{\gamma}, \quad (7)$$

where  $F_s$ ,  $F_n$ , and  $F_t$  are the sum of the forces in the tangential, normal, and binormal directions, respectively. A 2D version of these force balances has been derived by Alben *et al.* [53], where tangential and binormal forces were absent in their isolated fixed fibers. Equations (6) and (7) describe a system of coupled nonlinear ordinary differential equations, the solution to which will give the fiber curvature and torsion. To solve Eqs. (6) and (7) we still need closures for the forces  $F_s$ ,  $F_n$ , and  $F_t$ . While several studies have been dedicated to finding analytical solutions for the forces exerted by the fluid on either isolated flexible fibers, weakly flexible fibers, or fibers in a Stokes flow regime [39,52,53,55], analytical forms for the forces on moderately flexible fibers, settling inertially, in a suspension are not available. Therefore, we resort to our DNS for finding models for the tangential, normal, and binormal forces on fibers.

Figure 6 shows a typical distribution of forces on a fiber from DNS. The interaction of the fiber with other fibers, as well as the fluctuations in the flow field, cause a nonuniform distribution of the forces on the fiber. The tangential forces exhibit a singular behavior at the fiber ends. The normal forces and binormal forces vary rather smoothly along the fiber and exhibit local peaks. We also note that the forces on fibers have an average and a stochastic part, the latter arising from the fluctuations caused by the settling process in an inertial flow as well as by the interactions with other fibers. The stochastic part of the forces can be characterized by the standard deviation of the probability distribution functions (PDFs) of forces on all individual fibers. In the following section we first examine the average and standard deviation of forces from DNS and propose a model for them.

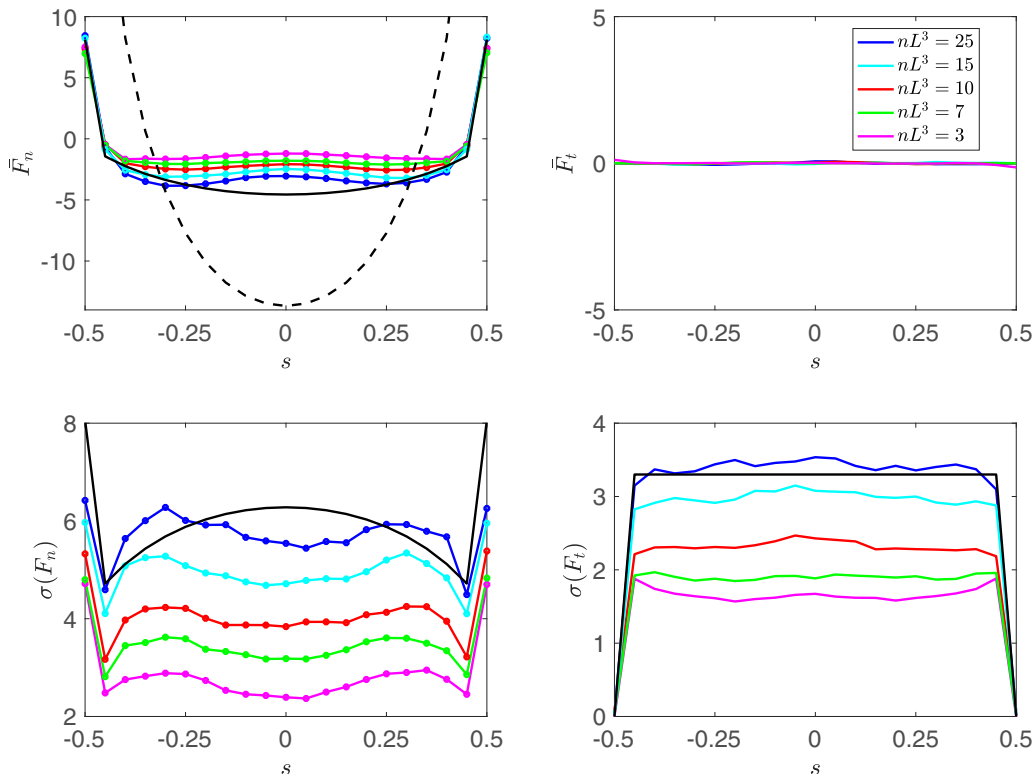


FIG. 7. Averages (top row) and standard deviations (bottom row) of the normal force,  $F_n$ , and the binormal force,  $F_t$ , along the fiber at  $\gamma = 0.1$  and  $Ga = 160$ . Dashed black lines show the original analytical solution of Xu and Nadim [52] and solid black lines show the modified analytical solutions, as explained in the text, for  $nL^3 = 25$ .

### A. Average and stochastic parts of fiber forces

The normal, tangential, and binormal forces on fibers can be split into an average and a stochastic part

$$F_n(s) = \bar{F}_n(s) + F'_n(s), \quad F_s(s) = \bar{F}_s(s) + F'_s(s), \quad F_t(s) = \bar{F}_t(s) + F'_t(s), \quad (8)$$

which also leads to a decomposition of  $f_s$  as  $f_s(s) = \bar{f}_s(s) + f'_s(s)$ . The constraints  $F'_t(-0.5) = F'_t(0.5) = 0$  and  $f'_s(-0.5) = f'_s(0.5) = 0$ , which are requirements of Eqs. (5) and (7), are placed on the stochastic parts of the forces. In this decomposition, the average parts of the forces are found from averaging over all the fibers in the domain and over several time steps (here we used a fixed number of fibers for averaging for all the simulations) and the stochastic part of the forces are the difference between the averaged and total forces on each individual fiber. In Fig. 7 we show the averages and standard deviations of the normal and binormal forces along the fiber length from DNS for different fiber concentrations at  $Ga = 160$ , and in Fig. 8 we show the averages and standard deviations of the tangential forces and the integral of the tangential force:  $f_s(s) = \int_{-0.5}^s F_s(\zeta) d\zeta$  for the same cases. The averages of the binormal forces are close to zero for all the cases. The magnitude of the averages of the normal and tangential forces and the standard deviations of the normal, tangential, and binormal forces increase monotonically with increasing  $nL^3$ .

Here, our goal is to find empirical models for estimating the averages and standard deviations of  $F_n$ ,  $F_s$ , and  $F_t$  by matching them with our DNS data. These models will be used in the stochastic reduced-order model that will be discussed in Sec. III C. Analytical solutions of  $F_n$  and  $F_s$ , for a single weakly flexible fiber settling in a Stokes flow, were derived by Xu and Nadim [52]. We

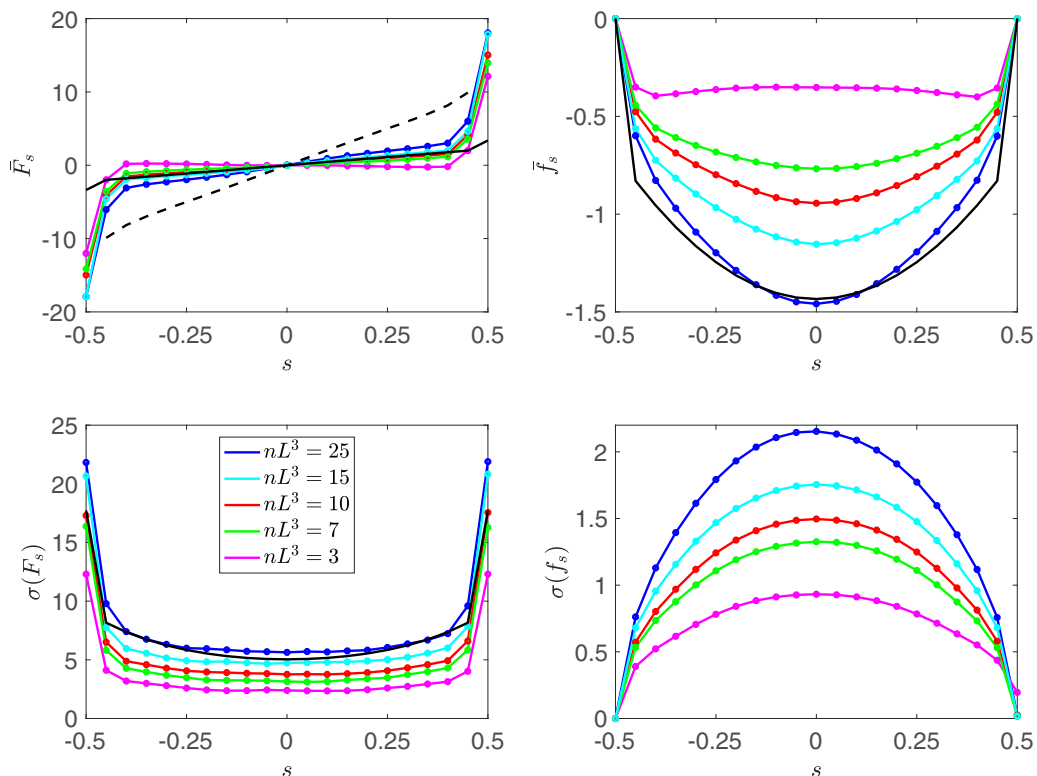


FIG. 8. Averages (top row) and standard deviations (bottom row) of the tangential force,  $F_s$ , and the integral of the tangential force,  $f_s$ , along the fiber at  $\gamma = 0.1$  and  $Ga = 160$ . Dashed black lines show the original analytical solution of Xu and Nadim [52] and solid black lines show the modified analytical solutions, as explained in the text, for  $nL^3 = 25$ .

compare these solutions to the averages of the forces from our DNS data in Figs. 7(a) and 8(a). In their original form, these solutions overestimate the magnitude of the forces on our inertial and moderately flexible fibers settling in suspensions. In addition, these analytical solutions are singular at the fiber ends. To obtain a good fit to our DNS forces and remove the singularities at the ends, we modify these analytical solutions by introducing compressed curvilinear coordinates and also by dividing the analytical forces by constants. The compressed curvilinear coordinate is defined as  $s_c = s/C(s)$ , where  $C(s) = 1.1$  at fiber ends, and  $C(s) = 1.5$  otherwise. By using these coordinates in the solutions of Xu and Nadim [52], the forces become more uniform along the fibers, which is a consequence of inertial effects and fiber-fiber interactions. We also divide the normal and tangential forces computed in these compressed coordinates by a constant that is 6 at  $Ga = 160$  and 24 at  $Ga = 40$ . The modified forces for estimating the averages of  $F_n$ ,  $F_s$ , and  $f_s$  (found from integrating the modified  $F_s$ ) are presented in Figs. 7(a), 8(a), and 8(b), and show functional forms that are close to the DNS data.

Next, inspired by the DNS results, we assume functional forms for the estimations of the standard deviation of  $F_n$ ,  $F_s$ , and  $F_t$  as follows. We observe that the standard deviation of the normal forces at any point on the fiber can be closely modeled as  $\sigma(F_n) = a_n|F_n| + C_n$ , where  $a_n$  and  $C_n$  are constants. The modeled  $\sigma(F_n)$  using this formulation that matches the DNS data at  $nL^3 = 25$  is shown in Fig. 7(c). Similarly, we observe that the standard deviations of  $F_s$  and  $F_t$  can be modeled as  $\sigma(F_s) = a_n F_n + C_s$  and  $\sigma(F_t) = C_t$ , with  $C_s$  and  $C_t$  being constants. The modeled standard deviations of  $F_s$  and  $F_t$  at  $nL^3 = 25$  are presented in Figs. 8(c) and 7(d), respectively. As will be discussed in

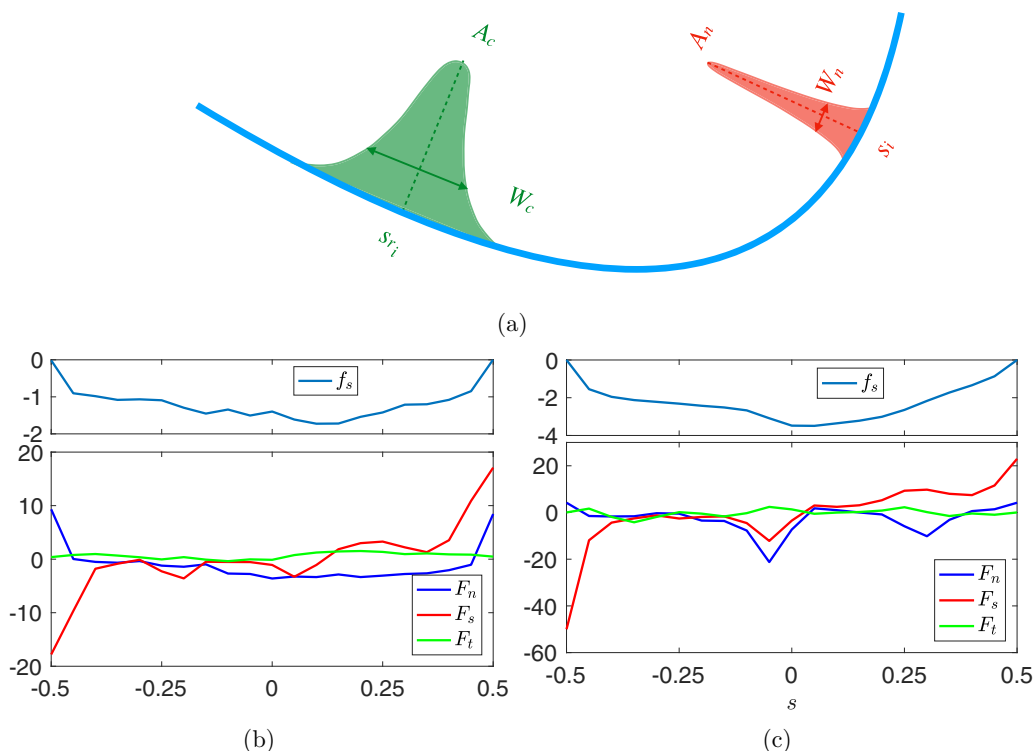


FIG. 9. (a) Schematic of the Gaussian kernels used to model forces due to fiber-fiber interactions and hydrodynamic fluctuations. (b), (c) An example of the distribution of the total forces along the fiber for the suspension with  $nL^3 = 25$  and  $\gamma = 0.1$  and  $Ga = 160$  generated by the stochastic model (b) and from DNS (c).

Secs. III B and III C, the constants  $a_n$ ,  $C_n$ , and  $C_s$  can be combined with other empirical constants in the total force to simplify the model.

It should also be noted that the trends of variations of the averages and the standard deviations along the fibers and their modeled forms at the data sets with  $Ga = 160$ ,  $\gamma = 0.05$  and  $Ga = 40$ ,  $\gamma = 0.1$  were very similar to those shown in Figs. 7 and 8. So, while not presenting the results here, we use the same models for estimating the averages and standard deviations of the forces as the ones discussed above in those data sets as well.

### B. Total force model

The total forces on each fiber can be modeled as the sum of a mean and a stochastic part, as stated in Eq. (8). As discussed in Sec. III A, we model the mean part of the forces using the modified analytical solutions. The stochastic part of the forces arises from the interactions with other fibers, similar to the particle-particle interactions in suspensions [56–59], and hydrodynamic fluctuations due to the inertial effects, similar to the fluctuations in hydrodynamic forces observed in the inertial settling of nonspherical particles [60–62]. To model these effects, we assume Gaussian kernel functions [see Fig. 9(a)]. The Gaussian kernel function has the property of smoothly distributing the effects of a local disturbance in forces on different numerical nodes on the fiber. In Fig. 9(a), the function with width  $W_c$  and height  $A_c$  represents a force due to the fiber-fiber interactions, including contacts and fluid-mediated interactions, and the function with width  $W_n$  and height  $A_n$  delineates a force due to hydrodynamic fluctuations. To choose proper length scales for  $W_c$  and

$W_n$ , we performed a fast Fourier transform (FFT) on the stochastic past of the normal component of the forces on the fibers from DNS. The averaged FFTs over all the fibers in each simulation exhibited two peaks at lengths  $5/21$  and  $1/21$ , with the latter being absent in the case of single fiber simulation. Therefore, we assigned these two values to the widths of Gaussian kernel functions as  $W_c = 5/21$  and  $W_n = 1/21$ . The amplitudes of the Gaussian kernel functions will be determined by minimizing the difference between the DNS and stochastic model results as will be explained in the following.

We assume that the stochastic part of the forces can be modeled as the sum of  $n_c$  Gaussian kernel functions that represent the disturbances to the forces due to fiber-fiber interactions and  $N$  ( $N = 21$  being the number of mesh points on each fiber) Gaussian kernel functions that represent the noise perturbations due to hydrodynamic fluctuations. For each fiber concentration, the probable number of fiber contacts or significant fluid-mediated hydrodynamic interactions,  $n_c$ , can be estimated from the average number of fibers that can be found in a sphere with a diameter of  $L$ , one fiber length. This number can be computed to be  $n_c = 1, 3, 5, 7, 12$ , and  $17$  for  $nL^3 = 3, 7, 10, 15, 25$ , and  $35$ , respectively. For a single fiber  $n_c = 0$ . The sum of the fiber-fiber interaction forcing and the noise forcing gives the stochastic part of the forces, expressed as

$$F'_n(s) = A_c^* \sum_{i=1}^{n_c} a_{r_i} \sigma [F_n(s_{r_i})] e^{(-|s-s_{r_i}|/W_c)} + A_n^* \sum_{i=1}^N b_{r_i} \sigma [F_n(s_i)] e^{(-|s-s_i|/W_n)}, \quad (9)$$

$$F'_s(s) = A_c^* \sum_{i=1}^{n_c} c_{r_i} \sigma [F_s(s_{r_i})] e^{(-|s-s_{r_i}|/W_c)} + A_n^* \sum_{i=1}^N d_{r_i} \sigma [F_s(s_i)] e^{(-|s-s_i|/W_n)}, \quad (10)$$

$$F'_t(s) = A_c^* \sum_{i=1}^{n_c} e_{r_i} \sigma [F_t(s_{r_i})] e^{(-|s-s_{r_i}|/W_c)} + A_n^* \sum_{i=1}^N f_{r_i} \sigma [F_n(s_i)] e^{(-|s-s_i|/W_n)}, \quad (11)$$

where  $A_c^*$  and  $A_n^*$  are the amplitudes of fiber-fiber interaction and noise forcing, respectively;  $a_{r_i}$ ,  $b_{r_i}$ ,  $c_{r_i}$ ,  $d_{r_i}$ ,  $e_{r_i}$ , and  $f_{r_i}$  are random numbers between  $-1$  and  $1$  that generate variations in the amplitudes of the forcing; and  $s_{r_i}$  is another random value between  $-1/2$  and  $1/2$  that generates a random location for the position of the fiber-fiber interaction. In summary, the model states that the stochastic part of the forces can be expressed as the sum of  $n_c$  randomly positioned fiber-fiber interaction forces, and  $21$  (the number of mesh points on each fiber) random forcings, positioned at each fiber mesh point. The amplitudes of these forcings randomly vary between  $-A_c^*$  and  $A_c^*$  and  $-A_n^*$  and  $A_n^*$ , respectively, and are also scaled by the local standard deviations of the forces. Other stochastic models for drag forces in particle-laden flows have been used in the literature [48–50], where similar to the present paper, fully resolved simulations have been used to inform the models for the stochastic part of the forces on particles.

Now we use the closures we found for the standard deviations of the force distributions on the fibers in Sec. III A to simplify the stochastic force part models in Eqs. (9)–(11) to

$$F'_n(s) = A_c \sum_{i=1}^{n_c} a_{r_i} |F_n(s_{r_i})| e^{(-|s-s_{r_i}|/W_c)} + A_n \sum_{i=1}^N b_{r_i} |F_n(s_i)| e^{(-|s-s_i|/W_n)}, \quad (12)$$

$$F'_s(s) = A_c \sum_{i=1}^{n_c} c_{r_i} F_n(s_{r_i}) e^{(-|s-s_{r_i}|/W_c)} + A_n \sum_{i=1}^N d_{r_i} F_n(s_i) e^{(-|s-s_i|/W_n)}, \quad (13)$$

$$F'_t(s) = A_c \sum_{i=1}^{n_c} e_{r_i} C_t e^{(-|s-s_{r_i}|/W_c)} + A_n \sum_{i=1}^N f_{r_i} C_t e^{(-|s-s_i|/W_n)}. \quad (14)$$

In this model, we have used a constant  $A_c = A_c^* a_n$  and dropped the  $C_n$  and  $C_s$  constants in the models for  $\sigma(F_n)$  and  $\sigma(F_s)$  for simplicity as we found they have an equivalent effect of varying  $A_c$  and  $A_n$

on the overall results. The advantage of the models in Eqs. (12)–(14) is that they only rely on three empirical constants,  $A_c$ ,  $A_n$ , and  $C_t$ , which makes the optimization process relatively simple.

Examples of modeled configurations of the total forces on a fiber are shown in Fig. 9(b). For comparison, examples of the forces from DNS are also presented in Fig. 9(c). The modeled and DNS forces show the same features in general. In both cases, the normal forces rise at the fiber ends, the tangential forces attain large values at the fiber ends, and the values of the binormal forces are small compared to the normal and tangential forces. For both modeled and DNS data, the local disturbances to the forces appear as local peaks that occur at the same location for all the three components of the forces, and have the same length scales between DNS and the model.

### C. Fiber shape model

Now, we focus on answering the second question: can we use the predictions for fiber forces to model the fiber shapes at different fiber concentrations? Using the stochastic models for  $F_n$ ,  $F_s$ , and  $F_t$  discussed in the previous sections, we first generate 15 000 different configurations for the forces on the fibers for each case, using different random values for  $a_{r_i}$ ,  $b_{r_i}$ ,  $c_{r_i}$ ,  $d_{r_i}$ ,  $e_{r_i}$ , and  $f_{r_i}$  for the forcing amplitudes, and  $s_{r_i}$  for the forcing location. We have also generated a probability density function that slightly favors the fiber ends for the location of fiber forcing. This is to take into account the higher probability of fiber ends to interact with other fibers. Next, for each forcing configurations we integrate Eqs. (6) and (7) numerically using a second order finite difference scheme to find the curvature  $\kappa$  and torsion  $\tau$  on each mesh point on the fiber. While the approximated functions for  $F_n$  and  $F_s$  provide a reasonably close representation of our DNS forces for the nodes in the interior of the fiber mesh, on the fiber ends the accuracy of these modeled functions is still compromised due to the singular nature of fiber forces. To overcome this problem, we follow the numerical steps below to integrate Eqs. (6) and (7).

(i) We apply the boundary conditions  $\kappa = 0$  and  $\tau = 0$  at both ends of the fiber and find  $\kappa(2)$  and  $\kappa(N - 1)$  using second order forward and backward schemes, respectively. These values are, however, inaccurate since  $F_n(1)$ ,  $F_n(N)$ ,  $f_s(s_1)$ , and  $f_s(s_N)$  have reduced accuracies. To correct for these, we multiply  $\kappa(2)$  and  $\kappa(N - 1)$  by a correction factor  $\alpha = 4$ , the value of which was found by matching the numerical and DNS values for  $\kappa(2)$  and  $\kappa(N - 1)$ .

(ii) We integrate Eqs. (6) and (7) by marching forwards from node 2 to  $N - 1$  and also by marching backwards from node  $N - 1$  to node 2 to find  $\kappa^{\text{forward}}$ ,  $\tau^{\text{forward}}$  and  $\kappa^{\text{backward}}$ ,  $\tau^{\text{backward}}$ , respectively. We find the intersection of  $\kappa^{\text{forward}}$  and  $\kappa^{\text{backward}}$  and assign the nodal values of  $\kappa^{\text{forward}}$  and  $\tau^{\text{forward}}$  to the nodes 2 to the point of intersection and the nodal values of  $\kappa^{\text{backward}}$  and  $\tau^{\text{backward}}$  to the nodes from the point of intersection to the node  $N - 1$  to find the final curvature and torsion values on all the nodes.

Once the curvature function  $\kappa(s)$  and the torsion function  $\tau(s)$  are known, the fiber shape coordinates can be found by numerically solving the following system of ordinary differential equations:

$$\frac{d}{ds} \begin{bmatrix} \mathbf{s}(s) \\ \mathbf{n}(s) \\ \mathbf{t}(s) \end{bmatrix} = \begin{bmatrix} 0 & \kappa(s) & 0 \\ -\kappa(s) & 0 & \tau(s) \\ 0 & -\tau(s) & 0 \end{bmatrix} \begin{bmatrix} \mathbf{s}(s) \\ \mathbf{n}(s) \\ \mathbf{t}(s) \end{bmatrix}, \quad (15)$$

$$\frac{d\mathbf{X}(s)}{ds} = \mathbf{s}(s). \quad (16)$$

The same transformation process as for DNS fibers is used to rotate the fibers from the original  $(x, z)$  frame to their  $(x', z')$  Frenet frame of reference.

In the numerical steps explained above, for the stochastic model to be complete, we still need to find the constants  $A_c$  and  $A_n$  and  $C_t$  that correspond to the strength of fiber-fiber interaction and random forces. To do so, we use a gradient descent optimization algorithm to minimize the difference between the results of the DNS and the stochastic model. In this regard, we define a measure of error for any parameter of interest,  $\xi$ , as follows. We generate the PDFs of  $\xi$  by

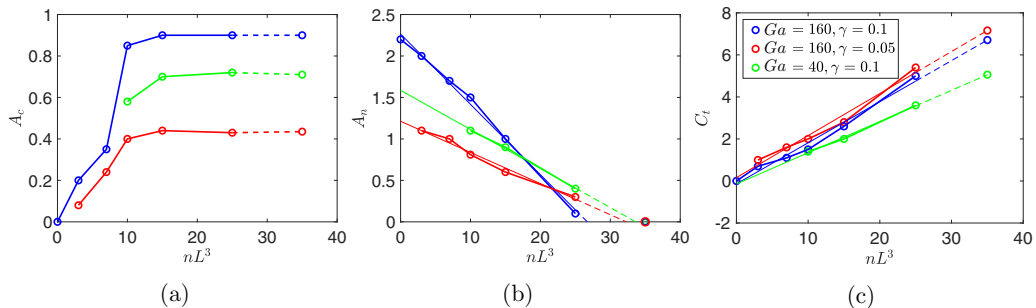


FIG. 10. Plots of the empirical constants used in the models to estimate the stochastic part of the fiber forces. Thin solid lines in (b) and (c) show linear fits. Values of  $A_c$ ,  $A_n$ , and  $C_t$  for  $nL^3 \leq 25$  are found by minimizing a cost function that measures the difference between DNS and model data, while the values at  $nL^3 = 35$  are extrapolations of the trends found for  $nL^3 \leq 25$ .

considering its variation over a fixed number of fibers (15 000 fibers in this case) both from the DNS and the stochastic model data. We define an error value for the parameter  $\xi$  as the difference between the PDFs (denoted  $F_{\text{prob. dist.}}$ ) of the DNS and stochastic model, normalized by the area under the DNS probability distribution function:  $E(\xi) = \int |F_{\text{prob. dist.}}^{\text{DNS}} - F_{\text{prob. dist.}}^{\text{model}}| d\xi / \int F_{\text{prob. dist.}}^{\text{DNS}} d\xi$ . We compute the error values for the following parameters: fiber end-to-end distance,  $d$ , fiber height,  $h$ , fiber out-of-plane height,  $l$ , averaged curvature along the fiber,  $\langle \kappa \rangle$ , maximum curvature along the fiber,  $\max(\kappa)$ , the standard deviation of curvature along the fiber,  $\sigma(\kappa)$ , averaged torsion along the fiber,  $\langle |\tau| \rangle$ , maximum torsion along the fiber,  $\max(|\tau|)$ , and the standard deviation of torsion along the fiber,  $\sigma(|\tau|)$ . We define a cost function as the sum of these errors and minimize this function using a gradient descent algorithm to find the optimized values of  $A_c$ ,  $A_n$ , and  $C_t$  that give the closest match between the DNS and stochastic model.

The optimized values of  $A_c$ ,  $A_n$ , and  $C_t$ , as presented in Fig. 10, have been obtained for fiber concentrations  $nL^3 \leq 25$  in each data set. At  $nL^3 = 35$ , we have extrapolated the trends found for  $nL^3 \leq 25$  to estimate the values of  $A_c$ ,  $A_n$ , and  $C_t$ . The amplitude  $A_c$ , representing the strength of fiber-fiber interaction forces, increases monotonically with fiber concentration, but reaches a plateau for  $nL^3 > 10$ . This is a threshold for transitioning from dilute to semidilute regime, where the mobility of fibers starts to be limited [29]. Therefore, at  $nL^3 = 35$ , we have simply assumed that  $A_c$  can be found as the average of the previous two data points. The amplitude  $A_n$ , that models the effects of hydrodynamic fluctuations, decreases linearly with increasing  $nL^3$  for  $nL^3 \leq 25$ . To extrapolate this linear trend to  $nL^3 = 35$ , however, we note that the fitted lines cross  $A_n = 0$  before reaching  $nL^3 = 35$  for all the cases and therefore we assume  $A_n = 0$  at  $nL^3 = 35$ . The amplitudes of  $A_c$  and  $A_n$  reveal the nature of the stochastic forces in each concentration regime. At low concentrations, the amplitude of fiber-fiber interaction forcing compared to noise forcing is small, and  $A_c = 0$  for the single fiber simulation. The stochastic part of forces at low concentrations mainly comes from the fluctuations in the hydrodynamics forces. For high fiber concentrations, on the other hand, the forcing due to fiber-fiber interactions becomes dominant and  $A_n$  linearly decreases until it reaches zero at high enough concentrations. The values of  $C_t$ , a measure of the strength of binormal forces, start from  $C_t = 0$  for the single fiber simulation, and increase linearly with  $nL^3$  for all the three simulated data sets. We use these linear extrapolations to find  $C_t$  values at  $nL^3 = 35$ . All coefficients  $A_c$ ,  $A_n$ , and  $C_t$  show the same trends for the three sets of simulations with different  $Ga$  and  $\gamma$  values. This indicates that the functional form of the stochastic model proposed here can be suitable for all these three data sets. The exact values of the plateaued values for  $A_c$  in Fig. 10(a), and the slopes of the linear regressions for  $A_c$  and  $C_t$  in Figs. 10(b) and 10(c), however, vary from case to case.

In Figs. 11–13, we present the PDFs of the fiber parameters at  $Ga = 160$ ,  $\gamma = 0.1$ , and different fiber concentrations, computed based on the DNS and the stochastic model. In these figures, for

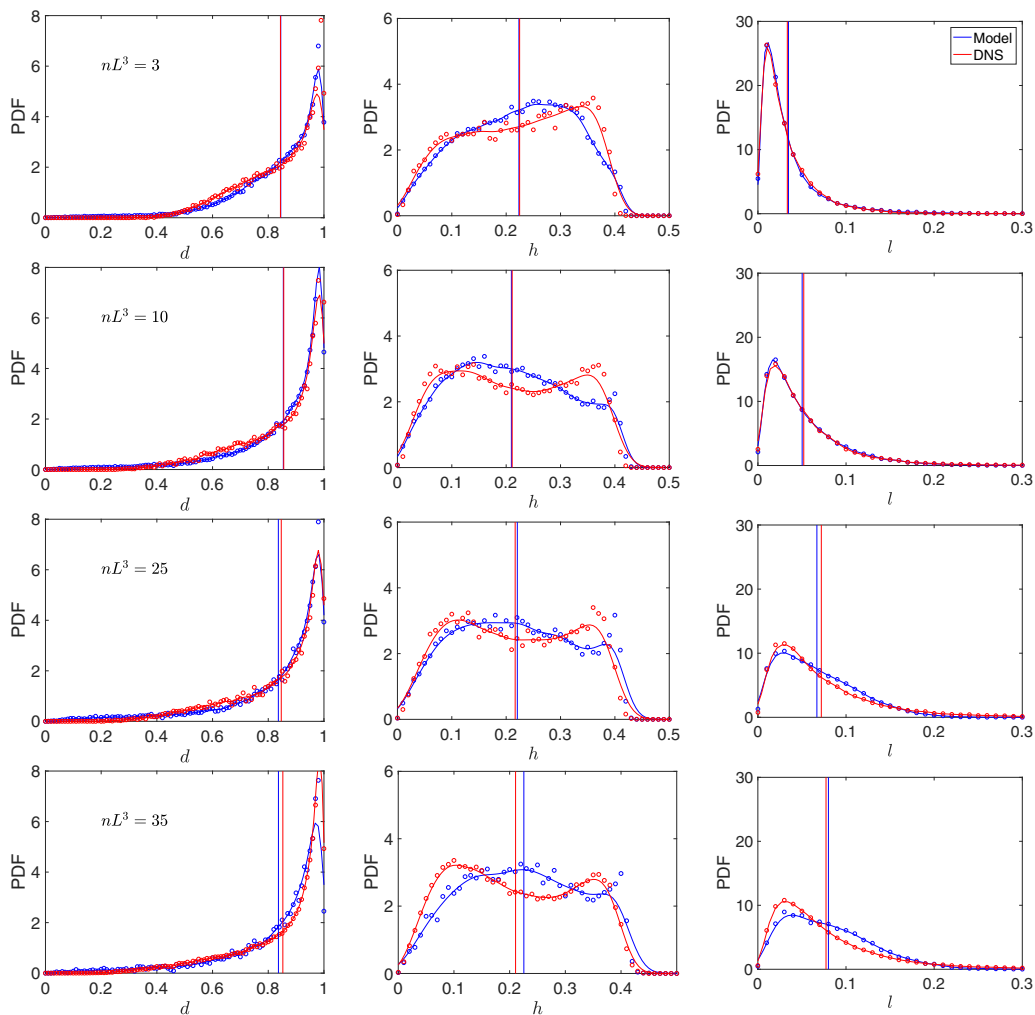


FIG. 11. PDFs of the fiber end-to-end distance,  $d$ , fiber height,  $h$ , and fiber out-of-plane height,  $l$ , for  $\gamma = 0.1$  and  $Ga = 160$  at different fiber concentrations:  $nL^3 = 3, 10, 25$ , and  $35$  (top to bottom rows) from DNS and the stochastic model. The circles delineate the PDFs from raw data, and the smoothed PDFs are indicated by solid lines. The vertical lines show the averages. At  $nL^3 = 35$ , the stochastic model uses the extrapolated empirical constants.

$nL^3 = 3, 10$ , and  $25$ , the constants  $A_n, A_c$ , and  $C_t$  used in the stochastic model were obtained by the optimization process explained above. At  $nL^3 = 35$ , to test the validity of the model beyond the set used for the optimization process, the stochastic model has used the extrapolated values of  $A_n, A_c$ , and  $C_t$ .

In terms of geometric properties,  $d, h$ , and  $l$ , as shown in Fig. 11, the DNS and stochastic model PDFs are close for  $d$  and  $l$ , and slightly different for  $h$ . Effects of increasing  $nL^3$  on the distribution of PDFs of  $d$ , as demonstrated by both DNS and model data, are mostly to shift PDFs toward higher values of  $d$  as the fiber mobility becomes limited at high fiber concentrations (see [29] for a more detailed discussion). As  $nL^3$  increases, the probability of finding fibers with lower heights increases, a trend which is also predicted by the model. Increasing the fiber concentration in the suspension significantly widens the PDFs of the fiber out-of-plane height, indicating that the fiber-fiber interactions induce more torsion. While this trend is correctly followed by the model as well,



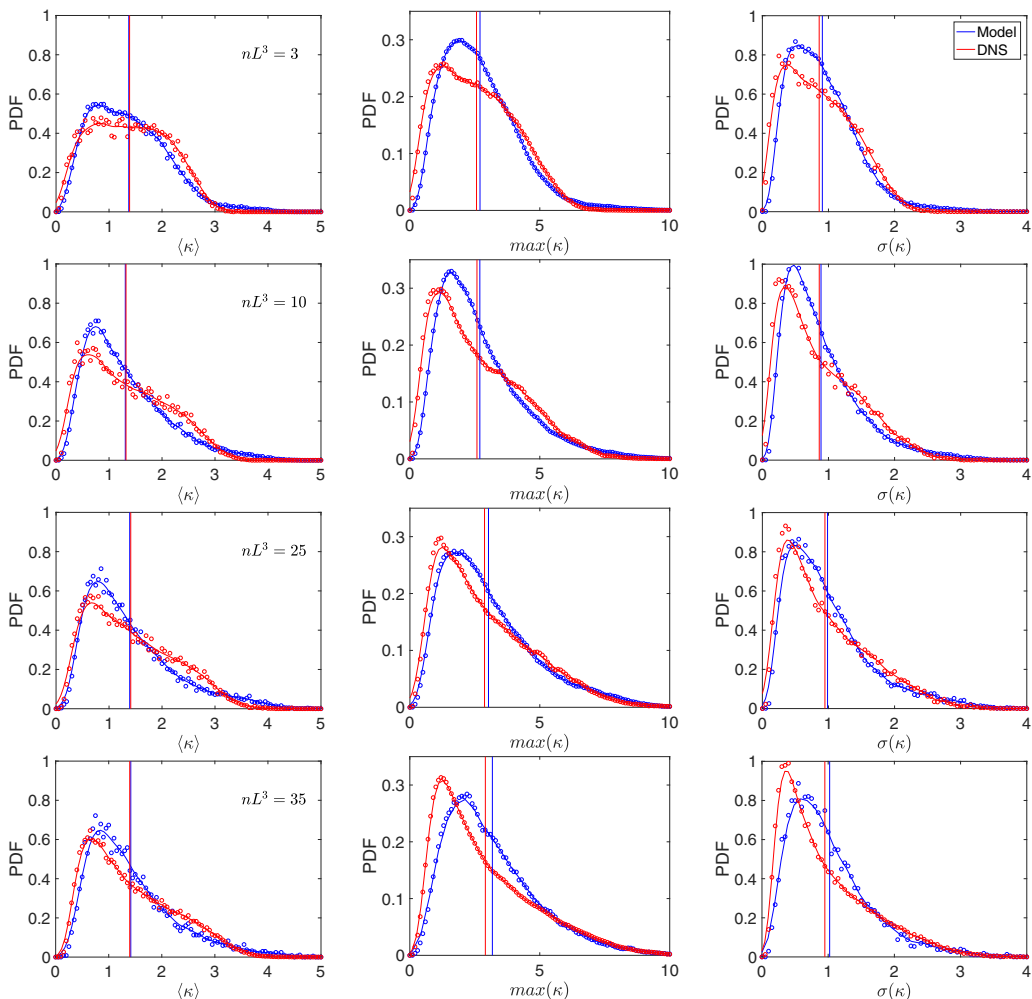


FIG. 12. PDFs of averaged curvature,  $\langle \kappa \rangle$ , maximum curvature,  $\max(\kappa)$ , and standard deviation of curvature,  $\sigma(\kappa)$ , on each fiber for  $\gamma = 0.1$  and  $Ga = 160$  at different fiber concentrations:  $nL^3 = 3, 10, 25$ , and  $35$  (top to bottom rows) from DNS and the stochastic model. The circles delineate the PDFs from raw data, and the smoothed PDFs are indicated by solid lines. The vertical lines show the averages. At  $nL^3 = 35$ , the stochastic model uses the extrapolated empirical constants.

the accuracy of the model is slightly reduced at  $nL^3 = 25$ . The averages of all the parameters in Fig. 11 are close between DNS and the model. The model with extrapolated constants at  $nL^3 = 35$  predicts the distribution and averages of PDFs of  $d$ ,  $h$ , and  $l$  fairly closely. The differences between the features of the PDFs from DNS and the model at this fiber concentration, particularly for  $h$  and  $l$  PDFs, can be due the general trend of the model slightly deviating from DNS results at higher concentrations, as also observed at  $nL^3 = 25$ .

For fiber curvature properties, as presented in Fig. 12, the DNS and model PDFs are fairly similar; they have very close averages, and follow the same trends for increasing fiber concentration. The PDFs from the stochastic model are, however, in general narrower than those from DNS, indicating that the model is creating less variations in curvature compared to DNS. Using extrapolated empirical constants at  $nL^3 = 35$  has not changed the accuracy of the model in predicting the curvature properties of the fibers. As for the PDFs of the absolute values of torsion, presented in

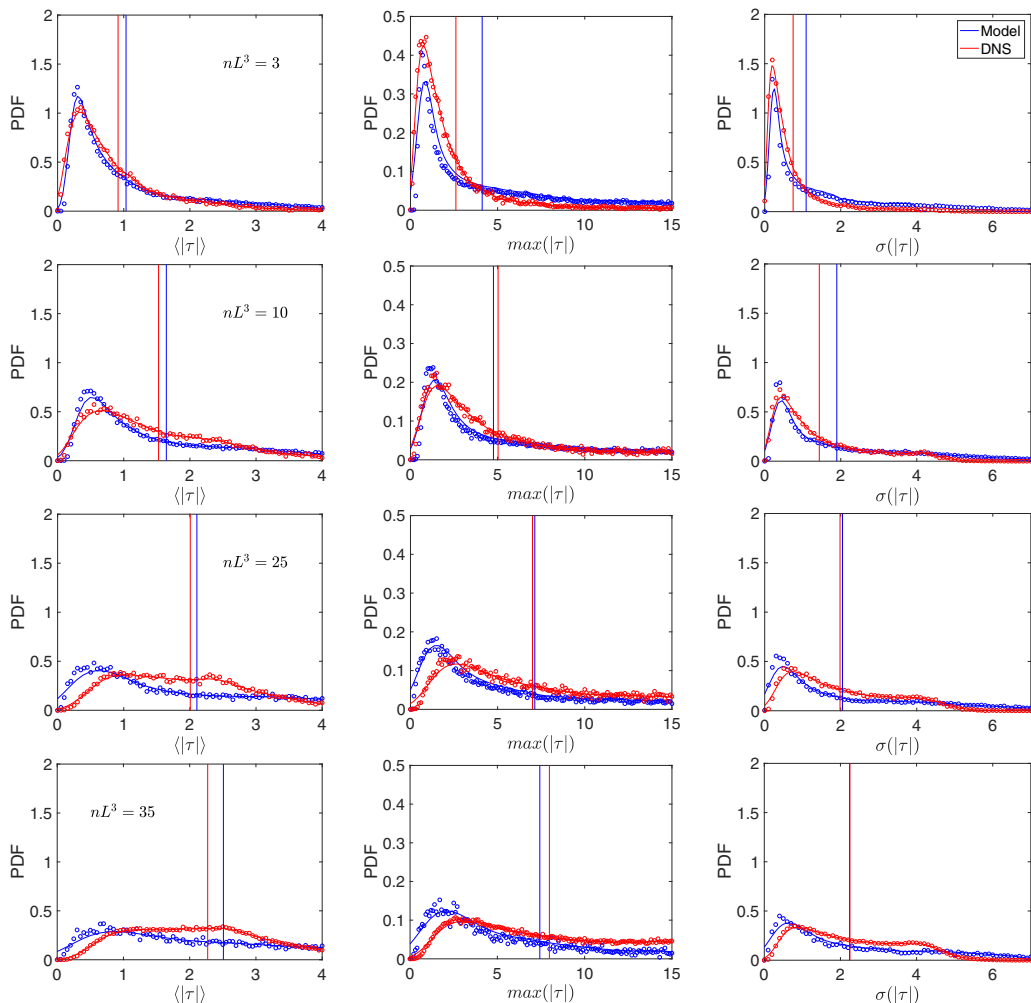


FIG. 13. PDFs of averaged absolute torsion,  $\langle |\tau| \rangle$ , maximum absolute torsion,  $\max(|\tau|)$ , and standard deviation of absolute torsion,  $\sigma(|\tau|)$ , on each fiber for  $\gamma = 0.1$  and  $Ga = 160$  at different fiber concentrations:  $nL^3 = 3, 10, 25$ , and  $35$  (top to bottom rows) from DNS and the stochastic model. The circles delineate the PDFs from raw data, and the smoothed PDFs are indicated by solid lines. The vertical lines show the averages. At  $nL^3 = 35$ , the stochastic model uses the extrapolated empirical constants.

Fig. 13, the agreement between DNS and the model varies depending on the fiber concentration and the quantitative metric used. Fiber torsion reached higher values compared to curvature, particularly at high fiber concentrations, and demonstrated more abrupt local variations. Therefore, minimizing the differences between torsion PDFs from DNS and the model was more challenging compared to geometric and curvature properties. The predictions of the model for the PDFs of  $|\tau|$  are reasonable for  $nL^3 = 3$  and  $10$ , although the averages of the PDFs do not match in all the cases. At  $nL^3 = 25$  and  $35$ , the DNS distribution of  $|\tau|$  is much wider and demonstrates long tails, indicating large variations in fiber torsion. Modeled PDFs follow these trends, but are biased towards smaller values. Despite these differences between the PDFs of  $|\tau|$ , the model is still capable of generating out-of-plane heights for the fiber shape that are close to DNS. The averages of the PDFs of  $|\tau|$  from DNS and the model are also close.

#### D. Validity of the model

An important question to address is how well the proposed stochastic model can predict the DNS results in different regimes where fiber concentration, inertia, and flexibility vary. While answering this question requires a large set of data, which is beyond the scope of this paper, in Fig. 5, we compare the averages of the fiber curvature, torsion, height, out-of-plane-height, and end-to-end distance from DNS and the model, for all the three data sets we have simulated. In this figure, for  $nL^3 \leq 25$ , the three empirical constants in the stochastic model have been found using an optimization process to minimize a cost function defined based on the differences between the DNS and the model, as explained in Sec. III C. At  $nL^3 = 35$ , the empirical constants are found by extrapolating the trends found for  $nL^3 \leq 25$ . This will allow us to test the validity of the model beyond the training set used for finding the empirical constants.

The difference between the averages of the shown parameters for all the cases, either with optimized or extrapolated constants, is less than 10%, with the trends being closely predicted by the model. When using the extrapolated constants, the model overpredicts fiber heights, but does not show a compromised accuracy in predicting other parameters. The accuracy of the model in predicting  $\langle \kappa \rangle$  and  $\bar{h}$  is lower for the single fiber simulation compared to the low concentration fiber suspensions at  $Ga = 160$  and  $\gamma = 0.1$ . The single fiber simulation reveals higher averaged curvature and height compared to the fibers in suspensions. At  $Ga = 160$  and  $\gamma = 0.05$ , where the fiber average curvature, torsion, and deformations are the highest, the accuracy of the model for  $\langle \kappa \rangle$ ,  $\langle |\tau| \rangle$ , and  $\bar{h}$  is slightly lower compared to their counterpart simulations in other data sets. These trends indicate that the accuracy of the model might in general be lower for cases where the fiber deformations are large, e.g., in cases where fiber flexibility or inertia significantly increases. Nonetheless, as mentioned above, these conjectures should be verified in future studies.

#### IV. SUMMARY AND CONCLUSIONS

In the present paper, we have investigated the shape of flexible fibers in inertially settling suspensions at different fiber concentrations, fiber flexibility, and inertia, using DNS coupled to an immersed boundary method for fiber-fluid coupling. Fibers' averaged curvature and height revealed a nonmonotonic dependence on fiber concentration,  $nL^3$ . In the dilute regime, with  $nL^3 < 10$ , fiber curvature and height decreased with increasing fiber concentrations as hindering of fiber settling velocities reduces the hydrodynamic forces on the fibers. For semidilute regimes, with  $nL^3 > 10$ , where hindering effects are reduced, averaged curvature and height showed a smaller dependence on  $nL^3$ . These parameters both increased for a higher value of fiber flexibility or inertia. Fiber torsion and out-of-plane height both increased monotonically with  $nL^3$  as the binormal forces are enhanced by fiber-fiber interactions and are not dependent on the gravitational forces. Fiber out-of-plane heights also increased with increasing fiber flexibility and inertia. While the out-of-plane fiber heights were smaller than fiber heights, their values were not negligible. Therefore, the planar shape assumption for fibers settling in suspensions may not be valid, particularly at higher fiber flexibility and higher fiber concentrations.

To understand the fiber shapes, we examined the forces on the fibers by splitting the total forces into mean and stochastic parts. The DNS results showed that the means of the normal and tangential forces along the fibers can be represented by a modified version of the analytical solutions found by Xu and Nadim [52] for a single weakly flexible fiber settling in a viscous fluid. The mean of the binormal forces was zero. To quantify the stochastic parts of the forces, we proposed closure models that consist of the sum of Gaussian kernel functions with amplitudes that scale with the local standard deviation of forces on the fiber. The Gaussian kernel functions represent interactions with other fibers and also random fluctuations in hydrodynamic forces due to inertial effects. The effects of random fluctuations were more significant compared to those of fiber-fiber interactions in dilute regimes ( $nL^3 < 10$ ). However, fiber-fiber interactions played a more important role in semidilute regimes ( $nL^3 > 10$ ).

Using the models for the mean and stochastic parts of fiber forces, we employed a reduced-order model to generate different three-dimensional (3D) shapes that fibers can adopt in suspensions of settling fibers at different fiber concentrations. A gradient descent algorithm was used to find the empirical constants needed for the reduced-order model, by minimizing error functions that were defined based on the differences between PDFs of different fiber parameters from DNS and the model. The predictions of the model were also tested for a higher fiber concentration using extrapolated empirical constants. The model could generate fiber shapes similar to those observed in DNS, with reasonably agreeing PDFs of fiber curvature, torsion, end-to-end distance, fiber height, fiber out-of-plane height, and fiber end-to-end distance. The similarity of fiber shapes between DNS and the model suggests that the forms of the forces we have assumed in the model are close representations of the forces on fibers in settling suspensions.

The present paper has investigated 3D geometric properties, curvature, and torsion of inertial settling fiber suspensions. We have proposed models for the forces on fibers in a suspension and explored the possibility of using these models to simulate the shape of the fibers. For future work, the validity of the models should be examined for a wider range of fiber flexibility, concentration, and inertia and for different flow settings to explore the possibility of extrapolating the model to parameter sets for which DNS is an expensive option. In addition, with our current flow solver, performing simulations at low  $Ga$  was not feasible. For future studies, the transitional effects of increasing  $Ga$  from viscous to inertial regimes on the fiber forces should be investigated.

#### ACKNOWLEDGMENTS

The authors are thankful for the insightful comments and suggestions by the two anonymous reviewers. L.B. acknowledges financial support from the Swedish Research Council (VR) via the multidisciplinary research environment INTERFACE, Hybrid multiscale modelling of transport phenomena for energy efficient processes, Grant No. 2016-06119.

#### APPENDIX: DETAILS OF THE FORCES IN THE IMMERSSED BOUNDARY METHOD

In our simulations, fluid and solid motions are coupled using an immersed boundary method [63]. In this approach, there are two sets of grid points: a fixed Eulerian grid  $\mathbf{x}$  for the fluid and a moving Lagrangian grid  $\mathbf{X}$  for the fibers. The volume force,  $\mathbf{f}$ , arising from the action of the filaments on the fluid is obtained by the convolution of the singular forces estimated on the Lagrangian nodes onto the Eulerian mesh; these are computed using the fluid velocity interpolated at the location of the Lagrangian points. We perform the interpolation and spreading using the regularized delta functions proposed by Roma *et al.* [64]. The fluid and solid equations are linked together by a hydrodynamic force:

$$\mathbf{F}_h = \frac{\mathbf{U}_{ib} - \mathbf{U}}{\Delta t}, \quad (\text{A1})$$

where  $\mathbf{U}_{ib}$  is the interpolated velocity on the Lagrangian points,  $\mathbf{U}$  is the velocity of the Lagrangian points, and  $\Delta t$  is the time step. The interpolation and spreading between the two grids are performed using the smooth delta function introduced by Roma *et al.* [64]:

$$\mathbf{U}_{ib} = \int_V \mathbf{u} \delta(\mathbf{X} - \mathbf{x}) dV, \quad (\text{A2})$$

$$\mathbf{f} = \rho_c \int_{L_f} \mathbf{F} \delta(\mathbf{X} - \mathbf{x}) ds, \quad (\text{A3})$$

where the factor  $\rho_c = \Delta \rho A_f (\rho_o L^2)$ , with  $A_f$  being the cross sectional area of the fiber, arises from choosing different scales for Eulerian and Lagrangian forces.

The lubrication model proposed by Lindström and Uesaka [65], for the lubrication force between two infinitely long cylinders, is used to include the short-range interactions between fibers. For

nonparallel cylinders, Yamane *et al.* [66] derived a first order approximation of the lubrication force:

$$\mathbf{F}_1^l = \frac{-12}{Ga \sin \theta} \frac{\dot{\zeta}}{\zeta}, \quad (\text{A4})$$

where  $\zeta$  denotes the shortest distance between the cylinders,  $\dot{\zeta}$  is the velocity along the shortest distance, and  $\theta$  is the angle between the axis of the two cylinders. This force is converted into a force per unit length, i.e., it is divided by  $\Delta s$ , the Lagrangian grid spacing such that it is applicable to the Euler-Bernoulli equations. Equation (A4) has a singularity for the case of parallel cylinders as  $\mathbf{F}_1^l \rightarrow \infty$  as  $\theta \rightarrow 0$ . For parallel cylinders, a first order approximation of the force per unit length was derived by Kromkamp *et al.* [67]:

$$\begin{aligned} \mathbf{F}_2^l &= \frac{-4}{\pi Gar_p^2} \left( A_0 + A_1 \frac{\zeta}{a} \right) \left( \frac{\zeta}{a} \right)^{-3/2} \dot{\zeta}, \\ A_0 &= 3\pi \sqrt{2}/8, \quad A_1 = 207\pi \sqrt{2}/160, \end{aligned} \quad (\text{A5})$$

where  $a$  is the radius of the cylinders ( $a = d/2$ ). Combining Eqs. (A4) and (A5), an approximation for the lubrication force for two finite cylinders can be derived [65] as

$$\mathbf{F}^l = \min(\mathbf{F}_1^l/\Delta s, \mathbf{F}_2^l). \quad (\text{A6})$$

In our simulations, when the shortest distance between two Lagrangian points becomes lower than  $d/4$ , we impose the lubrication correction  $\mathbf{F}^{\text{LC}} = \mathbf{F}^l - \mathbf{F}_0^l$ , with  $\mathbf{F}_0^l$  being the lubrication force at a distance of  $d/4$ . Finally, the total lubrication force acting on the  $i$ th element is obtained as

$$\mathbf{F}_i^{\text{LC}} = \sum_{j \neq i}^{Nl} \mathbf{F}_{ij}^{\text{LC}}, \quad (\text{A7})$$

where  $Nl$  is the number of Lagrangian points closer than the activation distance  $d/4$  to the  $i$ th point.

To avoid contacts and overlap between fibers, a repulsive force is also implemented. This has the form of a Morse potential [68], with a general form

$$\phi = D_e [ e^{-2\beta(r_f - r_e)} - 2e^{-\beta(r_f - r_e)} ], \quad (\text{A8})$$

where  $D_e$  is the interaction strength,  $\beta$  a geometrical scaling factor,  $r_f$  the distance between two elements on two different fibers, and  $r_e$  the zero cutoff force distance. The repulsive force between the elements  $i$  and  $j$  is the derivative of the potential function  $\phi$ :

$$\mathbf{F}_{ij}^c = \frac{d\phi}{dr} \mathbf{d}_{ij}, \quad (\text{A9})$$

where  $\mathbf{d}_{ij}$  is the unit vector in the direction joining the contact points. Finally, the total repulsive force on the  $i$ th element is obtained as

$$\mathbf{F}_i^c = \sum_{j \neq i}^{Nc} \mathbf{F}_{ij}^c, \quad (\text{A10})$$

where  $Nc$  is the number of Lagrangian points closer than the cutoff distance  $r_e$  to the  $i$ th point. As we consider moderate values of flexibility, we neglect the interaction of fibers with themselves. We also neglect contact frictional forces for all the cases in this paper.

---

[1] F. Lundell, L. D. Söderberg, and P. H. Alfredsson, Fluid mechanics of papermaking, *Ann. Rev. Fluid Mech.* **43**, 195 (2011).

- [2] L. Jiang, L. Gao, and J. Sun, Production of aqueous colloidal dispersions of carbon nanotubes, *J. Colloid Interface Sci.* **260**, 89 (2003).
- [3] J. D. Redlinger-Pohn, C. Brouzet, C. Aulin, A. Engstrom, A. V. Riazanova, C. Holmqvist, F. Lundell, and L. D. Soderberg, Mechanisms of cellulose fiber comminution to nanocellulose by hyper inertia flows, *ACS Sustainable Chem. Eng.* **10**, 703 (2022).
- [4] A. J. Gooday and C. M. Turley, Responses by benthic organisms to inputs of organic material to the ocean floor: A review, *Philos. Trans. R. Soc. A* **331**, 119 (1990).
- [5] S. Borodulina, H. R. Motamedian, and A. Kulachenko, Effect of fiber and bond strength variations on the tensile stiffness and strength of fiber networks, *Int. J. Solids Struct.* **154**, 19 (2018).
- [6] N. Provatas, M. J. Alava, and T. Ala-Nissila, Density correlations in paper, *Phys. Rev. E* **54**, R36 (1996).
- [7] E. Lushi, H. Wioland, and R. E. Goldstein, Fluid flows created by swimming bacteria drive self-organization in confined suspensions, *Proc. Natl. Acad. Sci. USA* **111**, 9733 (2014).
- [8] M. Shelley and J. Zhang, Flapping and bending bodies interacting with fluid flows, *Annu. Rev. Fluid Mech.* **43**, 449 (2011).
- [9] O. Du Roure, A. Lindner, E. N. Nazockdast, and M. J. Shelley, Dynamics of flexible fibers in viscous flows and fluids, *Ann. Rev. Fluid Mech.* **51**, 539 (2019).
- [10] B. Delmotte, E. Climent, and F. Plouraboué, A general formulation of bead models applied to flexible fibers and active filaments at low Reynolds number, *J. Comput. Phys.* **286**, 14 (2015).
- [11] M. Lagomarsino, I. Pagonabarraga, and C. Lowe, Hydrodynamic Induced Deformation and Orientation of a Microscopic Elastic Filament, *Phys. Rev. Lett.* **94**, 148104 (2005).
- [12] L. Li, H. Manikantan, D. Saintillan, and S. E. Spagnolie, The sedimentation of flexible filaments, *J. Fluid Mech.* **735**, 705 (2013).
- [13] I. Llopis, I. Pagonabarraga, M. C. Lagomarsino, and C. P. Lowe, Sedimentation of pairs of hydrodynamically interacting semiflexible filaments, *Phys. Rev. E* **76**, 061901 (2007).
- [14] B. Marchetti, V. Raspa, A. Lindner, O. Du Roure, L. Bergougnoux, E. Guazzelli, and C. Duprat, Deformation of a flexible fiber settling in a quiescent viscous fluid, *Phys. Rev. Fluids* **3**, 104102 (2018).
- [15] G. Saggiorato, J. Elgeti, R. G. Winkler, and G. Gompper, Conformations, hydrodynamic interactions, and instabilities of sedimenting semiflexible filaments, *Soft Matter* **11**, 7337 (2015).
- [16] X. Schlagberger and R. Netz, Orientation of elastic rods in homogeneous Stokes flow, *Europhys. Lett.* **70**, 129 (2005).
- [17] S. Allende, C. Henry, and J. Bec, Stretching and Buckling of Small Elastic Fibers in Turbulence, *Phys. Rev. Lett.* **121**, 154501 (2018).
- [18] C. Brouzet, G. Verhille, and P. Le Gal, Flexible Fiber in a Turbulent Flow: A Macroscopic Polymer, *Phys. Rev. Lett.* **112**, 074501 (2014).
- [19] A. Gay, B. Favier, and G. Verhille, Characterisation of flexible fibre deformations in turbulence, *Europhys. Lett.* **123**, 24001 (2018).
- [20] M. E. Rosti, A. A. Banaei, L. Brandt and A. Mazzino, Flexible Fiber Reveals the Two-Point Statistical Properties of Turbulence, *Phys. Rev. Lett.* **121**, 044501 (2018).
- [21] G. Verhille and A. Bartoli, 3D conformation of a flexible fiber in a turbulent flow, *Exp. Fluids* **57**, 117 (2016).
- [22] J. K. Wiens and J. M. Stockie, Simulating flexible fiber suspensions using a scalable immersed boundary algorithm, *Comput. Methods Appl. Mech. Eng.* **290**, 1 (2015).
- [23] P. J. Žuk, A. M. Słowicka, M. L. Ekiel-Jezewska, and H. A. Stone, Universal features of the shape of elastic fibres in shear flow, *J. Fluid Mech.* **914**, A31 (2021).
- [24] B. Chakrabarti, Y. Liu, J. LaGrone, R. Cortez, L. Fauci, O. Du Roure, D. Saintillan, and A. Lindner, Flexible filaments buckle into helicoidal shapes in strong compressional flows, *Nat. Phys.* **16**, 689 (2020).
- [25] A. Sabrio and M. Rasoulzadeh, Main modes of microfilament particles deformation in rough channels, *Phys. Fluids* **34**, 013320 (2022).
- [26] M. Bukowicki and M. L. Ekiel-Jezewska, Sedimenting pairs of elastic microfilaments, *Soft Matter* **15**, 9405 (2019).
- [27] L. H. Switzer and D. J. Klingenberg, Rheology of sheared flexible fiber suspensions via fiber-level simulations, *J. Rheol.* **47**, 759 (2003).

- [28] A. Perazzo, J. K. Nunes, S. Guido, and H. A. Stone, Flow-induced gelation of microfiber suspensions, *Proc. Natl. Acad. Sci. USA* **114**, E8557 (2017).
- [29] A. A. Banaei, M. Rahmani, D. M. Martinez, and L. Brandt, Inertial settling of flexible fiber suspensions, *Phys. Rev. Fluids* **5**, 024301 (2020).
- [30] P. Nakielski, S. Pawłowska, F. Pierini, W. Liwińska, P. Hejduk, K. Zembrzycki, E. Zabost, and T. A. Kowalewski, Hydrogel nanofilaments via core-shell electrospinning, *PLoS ONE* **10**, e0133458 (2015).
- [31] S. G. Advani and C. L. Tucker, The use of tensors to describe and predict fiber orientation in short fiber composites, *J. Rheol.* **31**, 751 (1987).
- [32] D. L. Koch, A model for orientational diffusion in fiber suspensions, *Phys. Fluids* **7**, 2086 (1995).
- [33] P. J. Krochak, J. A. Olson, and D. M. Martinez, The orientation of semidilute rigid fiber suspensions in a linearly contracting channel, *Phys. Fluids* **20**, 073303 (2008).
- [34] S. K. Kugler, A. Kech, C. Cruz, and T. Osswald, Fiber orientation predictions a review of existing models, *J. Compos. Sci.* **4**, 69 (2020).
- [35] C. Marchioli and A. Soldati, Rotation statistics of fibers in wall shear turbulence, *Acta Mech.* **224**, 2311 (2013).
- [36] K. Gustavsson and A. K. Tornberg, Gravity induced sedimentation of slender fibers, *Phys. Fluids* **21**, 123301 (2009).
- [37] B. Herzhaft and É. Guazzelli, Experimental study of the sedimentation of dilute and semi-dilute suspensions of fibres, *J. Fluid Mech.* **384**, 133 (1999).
- [38] J. Salmela, D. M. Martinez, and M. Kataja, Settling of dilute and semidilute fiber suspensions at finite Re, *AIChE J.* **53**, 1916 (2007).
- [39] H. Manikantan, L. Li, S. E. Spagnolie, and D. Saintillan, The instability of a sedimenting suspension of weakly flexible fibres, *J. Fluid Mech.* **756**, 935 (2014).
- [40] H. Manikantan and D. Saintillan, Effect of flexibility on the growth of concentration fluctuations in a suspension of sedimenting fibers: Particle simulations, *Phys. Fluids* **28**, 013303 (2016).
- [41] D. Dotto and C. Marchioli, Orientation, distribution, and deformation of inertial flexible fibers in turbulent channel flow, *Acta Mech.* **230**, 597 (2019).
- [42] D. Dotto, A. Soldati, and C. Marchioli, Deformation of flexible fibers in turbulent channel flow, *Meccanica* **55**, 343 (2020).
- [43] M. Alipour, M. De Paoli, S. Ghaemi, and A. Soldati, Long non-axisymmetric fibres in turbulent channel flow, *J. Fluid Mech.* **916**, A3 (2021).
- [44] M. Sulaiman, E. Climent, B. Delmotte, P. Fede, F. Plouraboué, and G. Verhille, Numerical modelling of long flexible fibers in homogeneous isotropic turbulence, *Eur. Phys. J. E* **42**, 132 (2019).
- [45] A. A. Banaei, M. E. Rosti, and L. Brandt, Numerical study of filament suspensions at finite inertia, *J. Fluid Mech.* **882**, A5 (2020).
- [46] B. Griffith, R. Hornung, D. McQueen, and C. Peskin, An adaptive, formally second order accurate version of the immersed boundary method, *J. Comput. Phys.* **223**, 10 (2007).
- [47] B. Griffith and N. Patankar, Immersed methods for fluid–Structure interaction, *Ann. Rev. Fluid Mech.* **52**, 421 (2020).
- [48] A. Esteghamatian, F. Euzenat, A. Hammouti, M. Lance, and A. Wachs, A stochastic formulation for the drag force based on multiscale numerical simulation of fluidized beds, *Int. J. Multiphase Flow* **99**, 363 (2018).
- [49] A. M. Lattanzi, V. Tavanashad, S. Subramaniam, and J. Capecelatro, Stochastic models for capturing dispersion in particle-laden flows, *J. Fluid Mech.* **903**, A7 (2020).
- [50] A. Seyed-Ahmadi and A. Wachs, Microstructure-informed probability-driven point-particle model for hydrodynamic forces and torques in particle-laden flows, *J. Fluid Mech.* **900**, A21 (2020).
- [51] S. Tenneti, M. Mehrabadi, and S. Subramaniam, Stochastic lagrangian model for hydrodynamic acceleration of inertial particles in gas–solid suspensions, *J. Fluid Mech.* **788**, 695 (2016).
- [52] X. Xu and A. Nadim, Deformation and orientation of an elastic slender body sedimenting in a viscous liquid, *Phys. Fluids* **6**, 2889 (1994).
- [53] S. Alben, M. Shelley, and J. Zhang, How flexibility induces streamlining in a two-dimensional flow, *Phys. Fluids* **16**, 1694 (2004).

- [54] P. Latil, L. Orgéas, C. Geindreau, P. J. J. Dumont, and S. R. Du Roscoat, Towards the 3d in situ characterisation of deformation micro-mechanisms within a compressed bundle of fibres, *Compos. Sci. Technol.* **71**, 480 (2011).
- [55] R. E. Khayat and R. G. Cox, Inertia effects on the motion of long slender bodies, *J. Fluid Mech.* **209**, 435 (1989).
- [56] A. M. Lattanzi, V. Tavanashad, S. Subramaniam, and J. Capecelatro, Stochastic model for the hydrodynamic force in Euler-Lagrange simulations of particle-laden flows, *Phys. Rev. Fluids* **7**, 014301 (2022).
- [57] M. Rahmani, A. Hammouti, and A. Wachs, Momentum balance and stresses in a suspension of spherical particles in a plane Couette flow, *Phys. Fluids* **30**, 043301 (2018).
- [58] A. Seyed-Ahmadi and A. Wachs, Sedimentation of inertial monodisperse suspensions of cubes and spheres, *Phys. Rev. Fluids* **6**, 044306 (2021).
- [59] G. Zhou and A. Prosperetti, Inertial effects in shear flow of a fluid-particle mixture: Resolved simulations, *Phys. Rev. Fluids* **5**, 084301 (2020).
- [60] D. Bi, T. Sun, Y. Wei, and X. Huang, On the dynamic behaviors of freely falling annular disks at different Reynolds numbers, *Phys. Fluids* **34**, 043307 (2022).
- [61] M. Rahmani and A. Wachs, Free falling and rising of spherical and angular particles, *Phys. Fluids* **26**, 083301 (2014).
- [62] A. Seyed-Ahmadi and A. Wachs, Dynamics and wakes of freely settling and rising cubes, *Phys. Rev. Fluids* **4**, 074304 (2019).
- [63] R. Mittal and G. Iaccarino, Immersed boundary methods, *Annu. Rev. Fluid Mech.* **37**, 239 (2005).
- [64] A. M. Roma, C. S. Peskin, and M. J. Berger, An adaptive version of the immersed boundary method, *J. Comput. Phys.* **153**, 509 (1999).
- [65] S. B. Lindström and T. Uesaka, Simulation of semidilute suspensions of non-Brownian fibers in shear flow, *J. Chem. Phys.* **128**, 024901 (2008).
- [66] Y. Yamane, Y. Kaneda, and M. Dio, Numerical simulation of semi-dilute suspensions of rodlike particles in shear flow, *J. Non-Newtonian Fluid Mech.* **54**, 405 (1994).
- [67] J. Kromkamp, D. T. M. Van Den Ende, D. Kandhai, R. G. M. Van Der Sman, and R. M. Boom, Shear-induced self-diffusion and microstructure in non-Brownian suspensions at non-zero Reynolds numbers, *J. Fluid Mech.* **529**, 253 (2005).
- [68] Y. Liu, L. Zhang, X. Wang, and W. K. Liu, Coupling of Navier–Stokes equations with protein molecular dynamics and its application to hemodynamics, *Int. J. Numer. Methods Fluids* **46**, 1237 (2004).